Computers in Biology and Medicine 143 (2022) 104948

Contents lists available at ScienceDirect

Computers in Biology and Medicine

journal homepage: www.elsevier.com/locate/compbiomed

A fully resolved multiphysics model of gastric peristalsis and bolus emptying in the upper gastrointestinal tract

Shashank Acharya [a], Sourav Halder [b], Wenjun Kou [c], Peter J. Kahrilas [c], John E. Pandolfino [c], Neelesh A. Patankar [a,b,*]

[a] Department of Mechanical Engineering, Northwestern University, Evanston, IL, 60208, USA
[b] Theoretical and Applied Mechanics Program, Northwestern University, Evanston, IL, 60208, USA
[c] Division of Gastroenterology and Hepatology, Feinberg School of Medicine, Northwestern University, Chicago, IL, 60611, USA

ARTICLE INFO

Keywords:
Esophagus
Stomach
Peristalsis
Fluid-structure interaction
Immersed boundary method
Incompressible multiphase flow
Biomechanics

ABSTRACT

Over the past few decades, *in silico* modeling of organ systems has significantly furthered our understanding of their physiology and biomechanical function. In spite of the relative importance of the digestive system in normal functioning of the human body, there is a scarcity of high-fidelity models for the upper gastrointestinal tract including the esophagus and the stomach. In this work, we present a detailed numerical model of the upper gastrointestinal tract that not only accounts for the fiber architecture of the muscle walls, but also the multiphasic components they help transport during normal digestive function. Construction details for 3D models of representative stomach geometry are presented along with a simple strategy for assigning circular and longitudinal muscle fiber orientations for each layer. We developed a fully resolved model of the stomach to simulate gastric peristalsis by systematically activating muscle fibers embedded in the stomach. Following this, for the first time, we simulate gravity-driven bolus emptying into the stomach due to density differences between ingested contents and fluid contents of the stomach. Finally, we present a case of retrograde flow of fluid from the stomach into the esophagus, resembling the phenomenon of acid reflux. This detailed computational model of the upper gastrointestinal tract provides a foundation for future models to investigate the biomechanics of acid reflux and probe various strategies for gastric bypass surgeries to address the growing problem of obesity.

1. Introduction and motivation

The digestive system is one of the main organ systems of the body and is responsible for ingestion, transport, breakdown and absorption of food necessary for normal body function. In spite of its importance, little attention has been paid to *in silico* modeling of this organ system compared to extensive modeling efforts for the cardiovascular, respiratory and skeletal systems of the human body. Modeling of organ systems can further our understanding of the role of biomechanical processes in these systems and help differentiate between physiological and pathological conditions. This can lead to improvements in treatment planning and overall outcomes. Up to this point, computational investigations of gastrointestinal biomechanics have focused on the fluid and solid problems separately [1–5]. Flow in the stomach was generated by fully specifying the motion of gastric walls with time [2,3] without accounting for the interaction between the elastic stomach wall structure and the internal fluid contents. While this approach reveals important details about flow fields in the stomach during gastric peristalsis [6,7], it provides little information on the relationship between pressure fields that drive flow and the material properties of the surrounding muscular structures. This information is valuable for probing the integrity of the muscle wall and relate measurable lumen pressures to material properties of the esophagus and stomach walls [8]. It must be noted that a significant amount of work has also been done to study the spread and absorption of pharmacological agents such as tablets and pills in the stomach [9–12]. Other numerical models of the gastrointestinal tract have accounted for electrical activity in the walls and the complex interaction between slow waves generated by the interstitial cells of Cajal, spike potentials and their overall role in eliciting contractions of the muscle wall [13–15]. However, the combined effect of contraction strength and the structure's material properties on the motion of the confined fluid contents remains to be explored.

In addition to the coupled fluid-solid phenomena observed during bolus transport and gastric mixing, it is important to note that the

* Corresponding author. Department of Mechanical Engineering, Northwestern University, Evanston, IL, 60208, USA.
E-mail address: n-patankar@northwestern.edu (N.A. Patankar).

https://doi.org/10.1016/j.compbiomed.2021.104948
Received 30 June 2021; Received in revised form 9 October 2021; Accepted 13 October 2021
Available online 15 October 2021

contents of the digestive system often include more than one homogeneous fluid. Air is often present in the gastric lumen and there are slight differences in the density of ingested food and the surrounding gastric fluid (which is similar to water). These density differences can significantly affect the internal flow fields. Therefore, it is important to capture the net effect of the elastic structure on the multiphasic components in any reasonably detailed model of the upper GI tract. In the upright position, gravity is often sufficient to cause fluid from the esophagus to empty into the stomach [16–18]. This necessitates the use of two fluid components to model gravity-driven emptying in the esophagus. In light of the studies summarized above, we aimed to develop a model that accounted for the complete two-way fluid-structure interaction (FSI) problem in the stomach along with a multiphasic approach that accounts for density differences observed during normal physiologic functioning of the upper GI tract.

2. Mathematical modeling of FSI and multiphase flow

2.1. Overview of the immersed boundary formulation and solution method

The computational model of the upper gastrointestinal tract presented in this work is an extension of the model previously developed and validated by Kou et al. [19–21] to analyze esophageal peristalsis and bolus transport using the immersed boundary method. Below, we summarize the mathematical formulation of the immersed boundary finite element (IBFE) method that was used to model the interaction between the fluid and solid components in this work. The IB method employs an Eulerian description for mass (incompressibility) and momentum conservation in the entire fluid-structure computational domain. For the hyperelastic structure, a Lagrangian approach is used to describe the solid's deformation and stress fields. Integral transforms that use Dirac delta function kernels exchange velocity and stress information between the two subdomains. Derivation of the continuum version of IB equations for a three-dimensional solid immersed in fluid is presented in Boffi et al. [22]. The discretized version of these equations were derived and implemented by Griffith and Luo [23]. The complete set of governing equations can be summarized as follows,

$$\frac{\partial \rho \mathbf{u}(\mathbf{x},t)}{\partial t} + \nabla\cdot[\rho \mathbf{u}(\mathbf{x},t)\mathbf{u}(\mathbf{x},t)] = -\nabla p(\mathbf{x},t) + \nabla\cdot\left[\mu\left(\nabla\mathbf{u}(\mathbf{x},t) + \nabla\mathbf{u}(\mathbf{x},t)^T\right)\right] + \rho\mathbf{g} + \mathbf{f}^e(\mathbf{x},t), \tag{1}$$

$$\nabla\cdot\mathbf{u}(\mathbf{x},t) = 0, \tag{2}$$

$$\mathbf{f}^e(\mathbf{x},t) = \int_U \mathbf{F}^e(\mathbf{s},t)\delta(\mathbf{x}-\boldsymbol{\chi}(\mathbf{s},t))\mathrm{d}\mathbf{s}, \tag{3}$$

$$\int_U \mathbf{F}^e(\mathbf{s},t)\cdot\mathbf{V}(\mathbf{s})\mathrm{d}\mathbf{s} = -\int_U \mathbb{P}^e(\mathbf{s},t) : \nabla_s\mathbf{V}(\mathbf{s})\mathrm{d}\mathbf{s}, \quad \forall\mathbf{V}(\mathbf{s}), \tag{4}$$

$$\mathbf{U}^e(\mathbf{s},t) = \int_\Omega \mathbf{u}(\mathbf{x},t)\delta(\mathbf{x}-\boldsymbol{\chi}(\mathbf{s},t))\mathrm{d}\mathbf{x}, \tag{5}$$

$$\int_U \frac{\partial\boldsymbol{\chi}}{\partial t}(\mathbf{s},t)\cdot\mathbf{V}(\mathbf{s})\mathrm{d}\mathbf{s} = \int_U \mathbf{U}^e(\mathbf{s},t)\cdot\mathbf{V}(\mathbf{s})\mathrm{d}\mathbf{s}, \quad \forall\mathbf{V}(\mathbf{s}), \tag{6}$$

$$\mathbb{P}^e = \mathcal{G}[\boldsymbol{\chi}(\cdot,t)]. \tag{7}$$

Here, Eqs. (1) and (2) describe momentum and mass conservation, respectively, of the entire fluid domain and the structures immersed within it. If ρ and μ are constant, these equations become identical to the Incompressible Navier-Stokes (INS) equations for a single fluid. As seen from the viscous term in Eq. (1), we assumed the fluid to be Newtonian even though most consumed foods are complex non-Newtonian fluids. We chose this modeling approach as water is the most common fluid used during clinical evaluation of esophageal motility. Unlike previous versions of the immersed boundary formulation used in Refs. [19,21] to model esophageal transport, Eq. (1) accounts for a variable density and viscosity that allows for more than one homogeneous fluid present in the domain. Eulerian and Lagrangian reference coordinates are labeled as $\mathbf{x}$ and $\mathbf{s}$, respectively. The combined multiphase fluid-structure system occupies the space $\Omega\subset\mathbb{R}^3$ and the structure's reference configuration occupies the space U. Velocity and pressure in the Eulerian description are denoted by $\mathbf{u}$ and p, respectively. The elastic force densities in the Eulerian and Lagrangian descriptions are denoted by $\mathbf{f}^e$ and $\mathbf{F}^e$, respectively. In the Lagrangian frame, the structure's current position, velocity and first Piola-Kirchoff stress are denoted by $\boldsymbol{\chi}(\mathbf{s},t)$, $\partial\boldsymbol{\chi}(\mathbf{s},t)/\partial t$ and $\mathbb{P}^e$, respectively. The structure's elastic force density is spread into the surrounding fluid using Eq. (3) which then affects fluid flow as seen from the presence of $\mathbf{f}^e$ in Eq. (1). Elastic force density from the structure $\mathbf{F}^e$ is computed using $\mathbb{P}^e$ and an arbitrary Lagrangian test function $\mathbf{V}(\mathbf{s})$ through a weak form of the principle of virtual work in Eq. (4). This is done by projecting $\mathbb{P}^e$ onto the finite-element space defined by $\mathbf{V}$. The intermediate Lagrangian velocity of the structure $\mathbf{U}^e$ is computed by interpolating fluid velocity using the delta function as shown in Eq. (5). This intermediate velocity is then projected into the space defined by $\mathbf{V}(\mathbf{s})$ using Eq. (6) to obtain the final Lagrangian velocity of the structure. The reason for this additional step is that the Eulerian equations are solved using the finite volume method whereas the Lagrangian equations are discretized using finite elements. As such, the intermediate velocity field must be projected onto the space defined by the finite element basis functions [24]. This final Lagrangian velocity is then integrated to obtain the updated position of the structure's nodes. The combination of Eqs. (5) and (6) ensures that the no-slip boundary condition is enforced at the fluid-solid boundary. The constitutive model of the structure is given by Eqn. (7) and is used to compute $\mathbb{P}^e$ from the current deformed configuration of the structure. Thus, Eqs. (1)–(7) illustrate the mathematical model used to capture the dynamics of the structure due to the surrounding fluid and vice versa. Complete details pertaining to the spatio-temporal discretization of the governing equations and the Eulerian-Lagrangian interaction equations, can be found in Refs. [19,21,23–25].

Briefly, the solution method consists of the following steps to obtain quantities $\boldsymbol{\chi}$ and $\mathbf{u}$ for the next time step $n+1$ from the quantities at the current time step n. First, the nodal locations of the Lagrangian structure are advanced by half a timestep using interpolated fluid velocity. Interpolation is achieved through the discrete version of Eq. (5) to compute an intermediate Lagrangian velocity field $\mathbf{U}^e$. Once this quantity is projected onto the basis functions used to describe the Lagrangian fields using Eq. (6), $\boldsymbol{\chi}^{n+1/2}$ is computed. With the updated configuration of the structure, solid stresses are computed and Eq. (4) is used to find the internal force density $\mathbf{F}$. This force is spread to the Eulerian domain using an operator $\mathcal{S}$ defined using Eq. (3) to find $\mathbf{f}^{n+1/2}$. Once the updated Eulerian spreading force is computed, the mass and momentum conservation equation for the entire computation domain Eqs. (1) and (2) are used to compute $\mathbf{u}^{n+1}$ and $p^{n+1/2}$. The domain is discretized using a Cartesian staggered-grid scheme with second-order accurate finite difference approximations for the divergence, gradient and Laplace operators. The convective term is discretized using the xsPPM7 version

of the Piecewise Parabolic Method (PPM) [26]. Temporal update of this nonlinear term is computed using the Adams-Bashforth method for the intermediate step. The second-order Crank-Nicolson scheme is used to handle the viscous, linear terms. Finally, the Lagrangian structure's nodal positions are corrected using the updated fluid velocity and an updated velocity restriction operator obtained by discretizing Eq. (6). In summary, to advance to the next timestep, the solution method consists of one force evaluation, one force spreading, two Lagrangian velocity computations and a solution of the Navier-Stokes equations. Additional details on the solution method can be found in the Supplementary Material. Complete mathematical details of the discrete operators derived from the continuous equations along with details on the preconditioned solver used to solve the conservation equations for the computational domain can be found in Refs. [23,24,26,27].

2.2. A brief description of the multiphase flow solver and interface treatment

As outlined in Sec. 2.1, the conservative form of the Navier-Stokes equations are used to model the overall fluid motion. Density and viscosity are functions of space and time in Eq. (1). As the material derivative of ρ remains zero, Eq. (2) is equivalent to the general form of the equation for conservation of mass in a continuum. This conservative form of the governing equations is discretized using a staggered grid approach with the traditional description of vector components defined on cell faces and scalar quantities defined at cell centers. By using mass flux density alongside the conservative form of the governing equations, the numerical scheme consistently transports mass and momentum which prevents any non-physical fluid motions. Special care is taken for the treatment of the nonlinear advection term which uses a third-order upwind scheme to maintain monotonicity with higher order accuracy. The overall fluid solver is second-order accurate for moderate density ratios as commonly observed in gastrointestinal flows. Complete details of the numerical implementation and tests for accuracy are provided in Refs. [25,27].

The interface between the two fluids of different density is tracked using the level-set method. In this study, the solid structures are assumed to be of the same density as the ambient fluid (water, unless mentioned otherwise). As such, no additional level set is needed to track the density field of the structure and it remains neutrally buoyant. A scalar function $\varphi(\mathbf{x}, t)$ denotes the value of the level set field in the domain. The variable φ is a signed distance function which satisfies the Eikonal equation $\|\nabla\varphi\| = 1$, and has a value of zero at the interface between the two fluids. The level set field is advected using the fluid velocity field with the equation

$$\frac{\partial\varphi}{\partial t} + \nabla\cdot(\varphi\mathbf{u}) = 0. \tag{8}$$

Fluid material properties are assigned based on the sign of φ at any given location. As is well known with traditional usage of level-set methods, linear advection leads to a gradual loss of the signed distance property $\|\nabla\varphi\| = 1$, of the φ field. Reinitialization is conducted at each time step by solving the following equation using a pseudo-time stepping scheme

$$\frac{\partial\varphi}{\partial\tau} + S(\varphi)(\|\nabla\varphi\| - 1) = 0. \tag{9}$$

This ensures that the advected level set field obeys the signed distance property at every stage. During reinitialization, although the φ field satisfies the $\|\nabla\varphi\| = 1$ property, it might lead to changes in the mass of individual phases. To avoid this error, an additional term that penalizes this mass loss is also solved to conserve the volume of each phase.

$$\frac{\partial\varphi}{\partial\tau} = -\Delta V. \tag{10}$$

Further details on the discrete versions of these equations along with additional analysis on diffusion and distortion at the fluid-fluid interface can be found in Nangia et al. [27].

2.3. Software implementation of the mathematical model

Computations using the governing equations previously described were performed using the IBFE and Multiphase Flow modules within the IBAMR open source framework [28] which is a distributed-memory parallel implementation of the IB method written in C++. Equations are solved on a Cartesian finite-volume grid with adaptive mesh refinement (AMR). Fluid variables and the AMR strategy are handled using data structures provided by the SAMRAI library [29] which uses a patch-based implementation approach. In addition to the zero level-set interface, the entire structure is located on the finest level of the finite volume grid. This ensures that both the fluid-solid interface and the zero-level set are described using the smallest possible mesh spacing for improved resolution. The structure is discretized using first-order finite elements and data related to Lagrangian operations is handled by the lib Mesh finite-element library [30]. The PETSc solver library [31] is used to compute numerical solutions for the discretized equation systems. The novel multiphase flow solver developed by Nangia et al. [27] used in this work has been extensively validated for a wide variety of benchmarks ranging from cases involving two fluids to Lagrangian structures interacting with the interface between two fluids. Details of the verification along with accuracy and convergence rates of the overall method can be found in Refs. [25,27]. Computations were performed using clusters PSC Briges-2 and SDSC Comet through the XSEDE program. Additional computations were conducted on the Northwestern University high performance computing cluster Quest. All simulations used 96 cores spread over four nodes unless mentioned otherwise.

3. Stomach geometry, associated fiber-architecture, and boundary conditions

3.1. Creating a solid model of the stomach

In Fig. 1, we show a few images of the human stomach as commonly seen in literature describing human anatomy. Such images formed the foundation for the construction of a 3D stomach structure. The geometry of the esophagus remains identical to the ones used in previous studies [19–21]. It consists of a thick-walled cylindrical tube with five layers, each having a distinct fiber architecture that corresponds to various mucosal and muscle layers in a human esophagus. The stomach geometry however, is far more complex and requires the construction of some key geometric elements which will then be used to generate the stomach structure.

It is clear from Fig. 1 that the human stomach has three primary structural features. The first being the rounded top known as the fundus. The second is the curved nature of the organ which leads to an upper and lower surface commonly known as the 'lesser' and 'greater' curvature. In the distal portion, there is a pyloric sphincter at the end of the stomach which controls and restricts the flow of fluid into the duodenum and small intestine for further digestion. Based on earlier studies, the cross-sectional area of the stomach is assumed to have an elliptical profile [21,34]. With these simplifications, we construct a set of planes that follow the center line of the stomach profile as shown in Fig. 2. This step is similar to the approach taken by Ferrua et al. [1] to construct a volume that depicts the stomach cavity. In the present study, we wish to create the muscle walls that envelope this cavity for our immersed structure. Each plane contains an elliptical cross section that is constructed using the lesser and greater curvatures as guidelines. Once the set of ellipses are available, they are used to create a sweep that generates the volume that serves as the stomach's cavity. With a similar operation, a larger volume is created that is the union of the cavity and the inner circular muscle layer. With a boolean subtraction operation, the cavity is excluded from the larger volume which results in the circular muscle

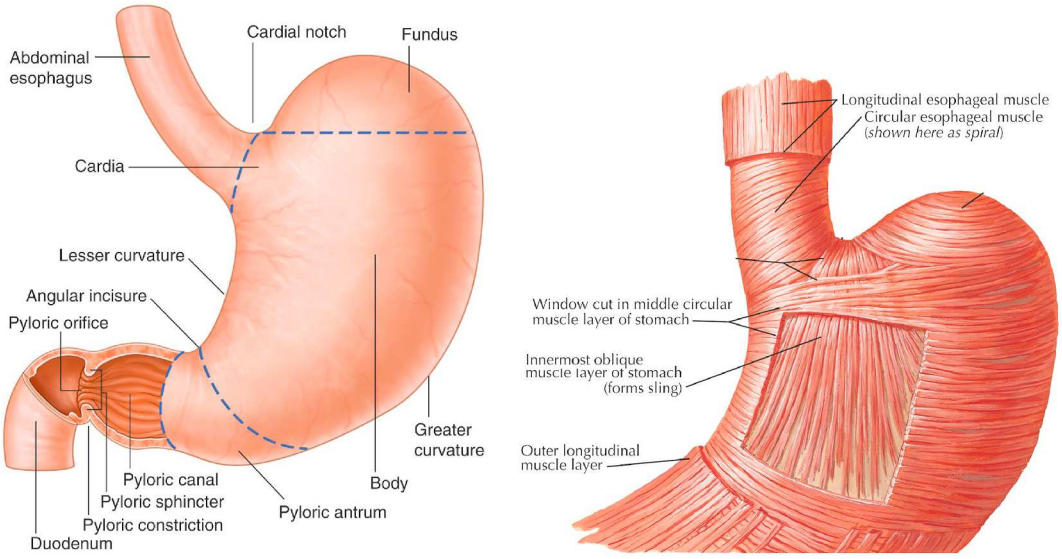

(a) Anatomical components of the stomach and cutaway showing the thicker gastric wall at the pyloric sphincter [32].

(b) Fiber orientations and muscle layers of the stomach. Muscle fibers from the esophagus continue to form the muscle layers of the stomach [33].

Fig. 1. Representative stomach geometry obtained from literature on upper gastrointestinal tract anatomy and biomechanics. These images highlight the primary geometric features of the stomach along with the orientations of fibers in the various muscle layers of the stomach walls. The three key geometric features are: 1) The fundus and its positioning with respect to the esophagus, 2) the lesser and greater curvatures of the stomach, and 3) the pyloric sphincter and its approximate muscle thickness. Images reproduced with permission from [32,33].

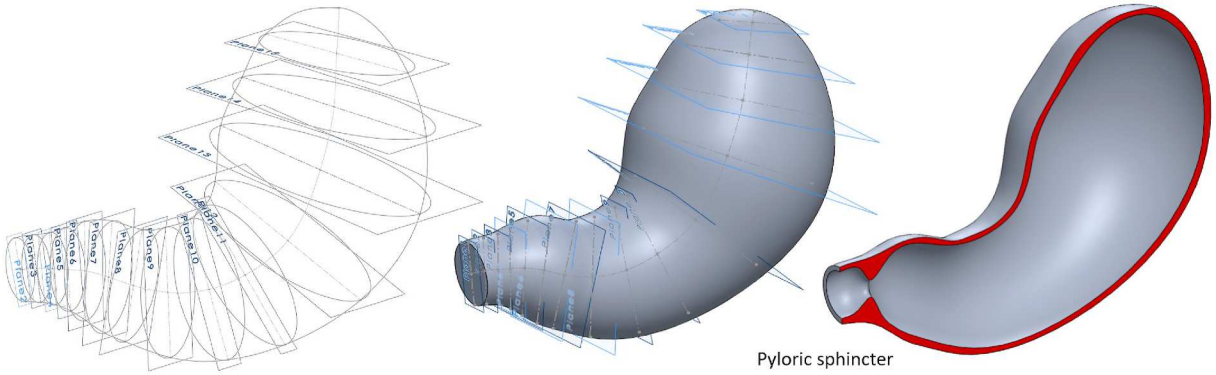

Fig. 2. Solid model of the stomach based on images from Fig. 1. The image on the left shows all the primitive geometric entities that were used to create the 3D volume. The three curves corresponding to the lesser curvature, greater curvature and the center line are visible. Also visible are the elliptical cross sections used to generate the stomach profile at distinct points along the centerline. The image in the middle shows the outer surface of the composite 3D volume which consists of the stomach cavity and the circular muscle layer. The rightmost image shows a cross sectional slice of the final structure used for the circular muscle layer. The thickness is highlighted in red. The structure is hollow which will be occupied by the fluid during IB simulations. This 3D model was created using SolidWorks R2018.

layer of the stomach wall. With a simple inflation operation, an outer thick-walled shell of this structure is created which serves as the longitudinal muscle layer of the stomach. Table 1 summarizes the dimensions of the structure used to describe the stomach model. With the construction of these two structures, the required geometry for creating a finite element mesh of the stomach's layers is complete. The esophageal structure is a thick walled cylinder and is meshed using Q1 hexahedral elements with trilinear basis functions. The number of elements in the axial, radial and circumferential directions are 120, 8 and 32, respectively. The cylinder's inner and outer diameters are 5 mm and 8 mm. The cylinder height is 9 cm. The mesh used for the stomach consisted of 189365 P1 tetrahedral elements with 41414 nodes. The dimensions of the stomach structure are provided in Table 1. All simulations were run with an adaptive time stepping scheme with a maximum time step of size 1.5×10^{-5} s and a maximum CFL number of 0.35 in the domain.

3.2. *Assigning fiber directions for the circular and longitudinal muscle layers*

In addition to geometric details, one must also consider the specific orientation of fibers within the stomach wall's muscle layers. During gastric peristalsis, these fibers contract in a systematic way to induce a propagating reduction in lumen area which then creates fluid flow within the stomach. As seen in Fig. 1, the stomach has three identifiable muscle layers: circular, longitudinal and oblique. They are named based on the orientation of fibers in each layer with respect to the centerline. Unlike the esophagus, these three stomach layers are not distinct from each other and fibers from one layer can continue on into another layer

Table 1
Dimensions of key features of the stomach model shown in Fig. 2. When empty, stomach volume is around 250 mL [40]. By choosing specific values for the lengths of the lesser and greater curvature, cavity volume is increased to resemble the stomach geometry after the consumption of a meal.

Geometric feature	Value	Source
Length of lesser curvature	22.16 cm	–
Length of greater curvature	33.25 cm	Ferrua et al. [2]
Length of the centerline	24.8 cm	–
Cavity volume	0.85 L	Ferrua et al. [36]
Widest diameter	9.5 cm	Schulze [37]
Pyloric sphincter diameter (relaxed)	1.6 cm	Deeg et al. [38]
Muscle layer thickness (both LM and CM)	2.75 mm	Liebermann-Meffert et al. [39]

Table 2
Complete set of activation timings and contraction strengths for each stomach plane used to simulate gastric peristalsis.

Plane num.	Activation begin time (t_a)	Activation end time (t_b)	Max. contraction strength (r_{max})	Plane status info
1	–	–	0.0	always inactive
2	–	–	0.0	always inactive
3	–	–	0.0	always inactive
4	1.0	1.5	0.2	–
5	1.25	1.75	0.3	–
6	1.5	2.0	0.4	–
7	1.75	2.25	0.5	–
8	2.0	2.5	0.5	–
9	2.25	2.75	0.5	–
10	2.5	3.0	0.5	–
11	2.75	3.25	0.5	–
12	0.0	–	0.2	pylorus plane (permanently active after t = 1.0 s)
13	–	–	0.0	always inactive
14	–	–	0.0	always inactive

in very complex ways. For the purposes of this study, we model only the circular and longitudinal muscle layers while acknowledging the fact that the oblique layer is equally important and has a significant effect on gastric peristalsis during normal function. In addition to these intricate muscle fiber orientations, the stomach has 'sling' fibers that have a significant effect on fluid entering the stomach through the esophagus. As these fibers are part of the oblique layer, they have not been implemented in this model. However their presence must be accounted for to make accurate predictions from the computational model.

To assign fiber directions for the circular muscle layer, we first generate a finite element mesh of the structure using the open source meshing software Gmsh [35]. This underlying mesh is used along with the planes defined in Fig. 2 to assign a fiber orientation for each element using a simple procedure. For every element in the mesh, the closest neighbor element with a face that lies on the solid's boundary is found. As the circular muscle layer is relatively thin, such a neighbor is relatively close to any element under consideration. The sides of this face are oriented along the surface of the solid structure. A projection of one of these sides on the plane closest to this element gives us the orientation of the circular muscle fiber for this element. An example of this step is shown in Fig. 3. With the help of the boundary face, we obtain vectors that are tangential to the surface. Projecting these tangent vectors onto the planes that define the circular profiles gives us a vector that is tangential to this circle. This procedure is repeated for every element in the mesh which results in the final fiber architecture for the circular muscle layer as seen in Fig. 3. During meshing, additional elements were added via local mesh refinement at the pyloric sphincter region to better capture the small diameter profile and its thicker walls. This leads to a greater density of fibers at the location of the sphincter as is evident in the rightmost image of Fig. 3.

For the longitudinal muscle layer fiber orientation, we first generate a set of guide curves that travel along the surface of the stomach. Manually placed points that lie on the outer surface of the stomach are joined using 3D splines. Using each curve's trajectory, tangent directions are computed for several equally spaced points on these curves as seen in Fig. 4. Following this step, for each element center, we identify two curves that are closest to it. Points on these curves that are closest to the element center are found and the average of the tangent vector for each of these points is assigned as the fiber orientation for said element. This ensures that fibers are generally oriented along the trajectories of the guide curves and there is a smooth variation of fiber vectors across all the elements in the layer. This process of assigning longitudinal fiber directions and the final fiber orientations obtained is visualized in Fig. 4.

3.3. Strain energy functions for the matrix and fiber components of the stomach wall

In this section, we summarize the constitutive relations and material properties used to describe the matrix and fiber components for the two muscle layers of the stomach wall. Like most continuum mechanics-based models of muscular tissue, each layer is assumed to be similar to a composite material that consists of anisotropic fibers embedded in an isotropic tissue matrix. Based on previous studies of esophageal transport by Kou et al. [19], we use the bi-linear constitutive model proposed by Yang et al. [41] to describe the behavior of the circular and longitudinal muscle layers of the gastric wall. Material constants applicable to the gastric wall are similar to the values chosen for the esophageal wall in Kou et al. [19] It should be noted that there are significant differences in material properties of the esophagus' circular

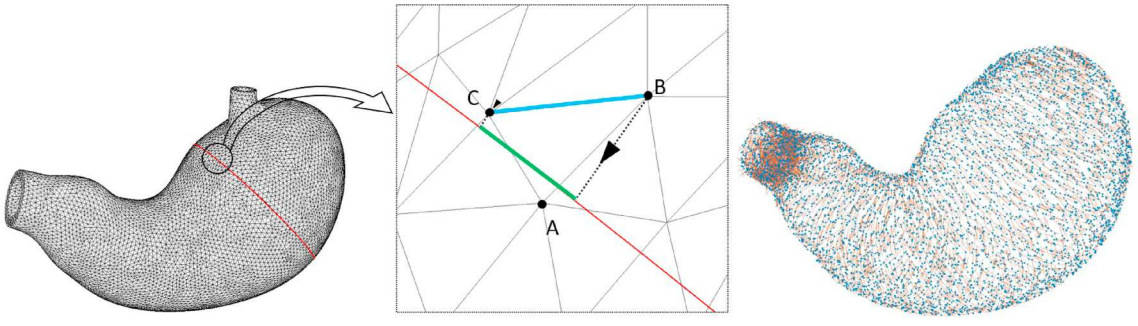

Fig. 3. A demonstration of assigning the circular muscle fiber orientation for an element using neighboring sides located on the solid boundary. The face ABC lies on the surface. Each of its sides are tangents to the solid surface. By projecting one of these tangents on to the plane, we obtain the fiber orientation for this element (shown in green). Image on the right shows the final fiber architecture for the circular muscle layer. Blue dots indicate element centers and brown lines indicate the element's fiber direction.

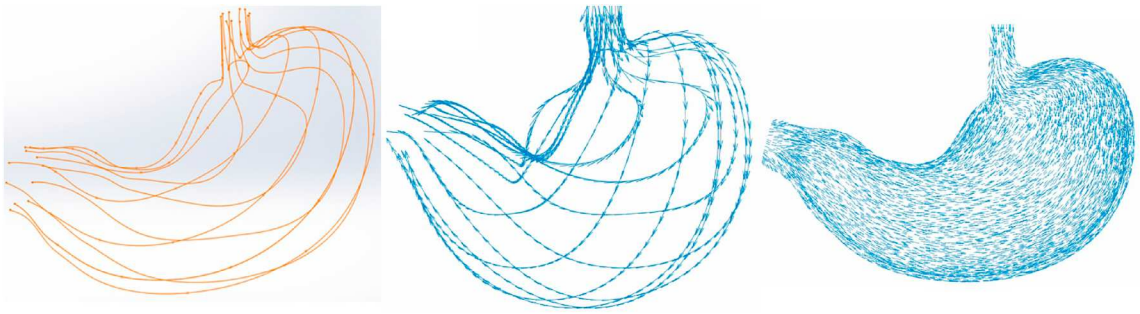

Fig. 4. Assigning fiber orientations to elements in the longitudinal muscle layer. Left: Guide curves drawn on the stomach surface. Center: Tangents to the guide curves used to assign fiber orientations to each element in the mesh. Right: Visualizing longitudinal fiber orientations for all elements in this muscle layer.

and longitudinal muscle layers compared to the corresponding muscle layers of the stomach wall [8]. However, as fibers in the stomach originate from respective muscle layers in the esophagus [33], we choose the same material properties as a first order approximation of the system. The strain energy function ψ for each layer of the stomach structure is thus written as the sum of two parts

$$\psi = \psi_{\text{matrix}} + \psi_{\text{fiber}}, \tag{11}$$

which uses the incompressible neo-Hookean constitutive model for the isotropic matrix and a bi-linear fiber model with orientation **a** for individual fibers. The orientation vector **a** is a function of **s** and its distribution was summarized in Figs. 3 and 4. The complete expression for ψ used for the circular (CM) and longitudinal (LM) layer, respectively can be written as

$$\psi_{\text{CM/LM}} = \psi_{\text{matrix}} + \psi_{\text{fiber}} = \frac{C_{\text{CM/LM}}}{2}(I_1 - 3) + \frac{C'_{\text{CM/LM}}}{2}\left(\frac{\sqrt{I_4}}{\lambda_{\text{CM/LM}}} - 1\right)^2. \tag{12}$$

Here, the first invariant of the right Cauchy-Green strain tensor $\mathbb{C}$ is denoted as I_1 and the magnitude of stretch of an individual fiber is denoted as $I_4 = \mathbb{C} : (\mathbf{a} \otimes \mathbf{a})$. The non-dimensional rest length of a CM or LM fiber is denoted by $\lambda_{\text{CM/LM}}$ and its default value is 1.0, indicating that the reference configuration of the element is equivalent to its undeformed shape. Muscular contractions are generated by systematically reducing these rest lengths to a value less than 1. The element then contracts to achieve a zero stress-state, thus reducing the length of the fiber as is observed during a muscular contraction. The following values were chosen for the material constants occurring in Eqn. (12): $C_{\text{CM/LM}} = 0.4$ kPa, and $C'_{\text{CM/LM}} = 4.0$ kPa.

For immersed boundary methods involving elastic solids, it has been observed that the divergence-free property of the fluid velocity is lost when this Eulerian variable is interpolated onto the Lagrangian domain through the discrete version of Eq. (5). In addition to this, errors occurring during time integration can also lead to changes in volume of the structure [19,23,42]. In this work, we employ the stabilization method proposed by Vadala-Roth et al. [24] to reinforce the incompressibility constraint in the solid domain. This is done by using modified invariants in the strain energy functions given above and by using an additional term $\mathbb{P}_{\text{dil}} = 2\beta_s J(J-1)\mathbb{F}^{-T}$. Here, β_s is a numerical bulk modulus with J being the determinant of $\mathbb{F}$, the deformation gradient. With this combination of modified invariants along with an additional stress to penalize volumetric changes, the overall method is observed to be more robust and is able to handle large elastic deformations without unphysical distortions in the finite element mesh.

3.4. Boundary conditions

In order to apply the immersed boundary method, the entire structure, which includes the esophagus and the stomach, was immersed in the fluid as shown in Fig. 5. The fluid domain is in the form of a cuboid with dimensions 300 mm × 150 mm × 295 mm. We specified zero-velocity Dirichlet boundary conditions at all the six outer faces of the fluid domain. The viscosity of the fluid was 0.01 Pa ·s. Based on the different applications discussed in the next section, the fluid density varies between 0.9 and 1.5 g/cm^3. To simulate gastric peristalsis, the structure included only the stomach, and a shorter fluid domain with a height of 250 mm was used. The boundary conditions for the fluid domain were identical for all examples.

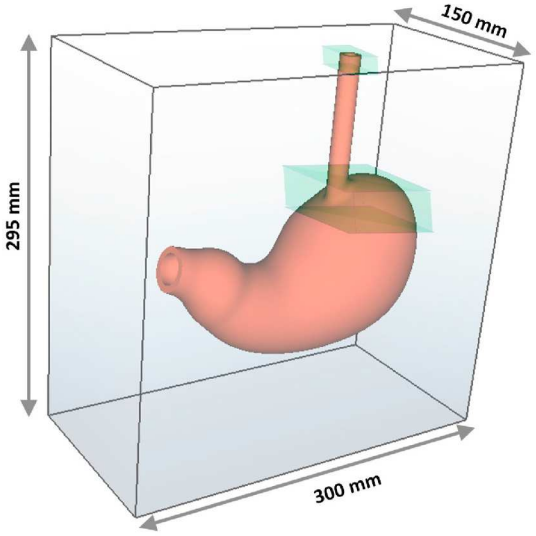

Fig. 5. Stomach model immersed in a fluid medium. The fluid domain takes the form of a cuboid with the velocity specified as zero at its 6 outer surfaces. Also shown are the lengths of the fluid domain in each direction. The domain is adaptively meshed using three AMR levels. The finest level provides an effective domain resolution of 200 × 100 x 196 cells in the x-, y- and z-direction, respectively. For the solid structure, portions of the finite-element mesh in the green boxes were held fixed using a penalty tethering force applied to the nodes. This provided support to the overall structure during fluid flow.

4. Application of gastroesophageal modeling principles to simulate commonly observed physiological processes

In the previous sections, we outlined the formulation and construction of the building blocks needed to model physiological processes in the upper gastrointestinal tract. In this section, we systematically assemble these models to showcase three examples of gastrointestinal motility and fluid flow observed due to the motion of the esophagus and stomach's walls.

4.1. Example 1: simulation of flow and wall motion during gastric peristalsis

In the first application of the concepts outlined above, we present muscular contraction-induced gastric peristalsis in a closed stomach. Unlike previous studies, gastric peristalsis is induced not by specifying the kinematics or time-varying nodal positions of the stomach wall, but by activating muscle fibers within the elastic structure to reduce lumen area. As explained in Sec. 3.3, contractions can be induced by locally reducing the value of λ. By varying this value along the stomach walls in a controlled manner, we can generate a contraction that travels from the body of the stomach, towards the pylorus. For this example, we assume that the stomach is closed and is filled with a homogeneous fluid similar to water but with a higher viscosity ($\mu = 0.01$ Pa ·s). These fluid properties are identical to the ones used to study the transport of a bolus from the esophagus into the stomach in Kou et al. [21].

Due to the complexity of the stomach's geometry, it is not possible to use a straightforward mathematical expression to reduce λ in a wave-like manner to induce peristalsis. To achieve peristalsis, we 'activate' the planes defined in Fig. 2 in a sequential manner to contract elements that are near specific planes. First, we activate the plane that spans the thickest part of the pyloric sphincter. This ensures that the sphincter is closed and does not allow any fluid to leave the cavity. This is similar to the normal functioning of the stomach where the pylorus offers a very high resistance to flow so that mixing is optimum before fluid enters the intestine [43]. Subsequently, each plane starting from the body of the stomach is activated one after the other. When a plane is activated, all elements near it have their rest lengths changed using the following expression:

$$r_{\text{curr}} = r_{\max} \exp\left(-\frac{1}{2\sigma^2} \left(\frac{t - t_{\text{avg}}}{t_b - t_a} \right)^2 \right). \tag{13}$$

Here, $(1 - r_{\text{curr}})$ is the activated value of λ and $(1 - r_{\max})$ is the smallest value of λ which occurs when the contraction strength is at its peak at any given location. Each plane is active for time interval $t_a \leq t \leq t_b$ and $t_{\text{avg}} = (t_a + t_b)/2$. The exponential function with $\sigma = 1$ ensures that elements near inactive planes have $r_{\text{curr}} \approx 0$ and as t exceeds t_b, r_{curr} gradually goes back to zero. This ensures that the contraction travels smoothly along the stomach. It should be noted that the contraction intensity of all elements activated by each plane is uniform and is not a function of distance of the element from the plane.

Velocity and pressure fields observed during gastric peristalsis are shown in Figs. 6 and 7, respectively. With the pylorus partially closed, circular muscle contractions force fluid towards the distal part of the stomach. Due to the contraction acting on a confined fluid, fluid is forced to travel in a retrograde direction with respect to the traveling peristaltic wave. This formation of a 'jet' is well reported in numerical and clinical studies of digestion in the stomach and our model reproduces this behavior as well. Although the rest length of fibers in the pyloric sphincter are reduced to induce closure, the pyloric sphincter is not fully closed. This leads to a small amount of fluid to exit the stomach cavity during peristalsis. This is similar to emptying in the stomach where a majority of the contents are forced back towards the proximal region and a small volume of fluid leaves to enter the duodenum.

4.2. Example 2: simulation of gravity-driven bolus emptying

Ingested food enters the stomach by traveling along the esophageal lumen and across the esophagogastric junction (EGJ). In the previous sections, we outlined the construction of the stomach geometry and simulation of gastric peristalsis. In this section, we combine this model with our previously developed model for the esophagus [19,21] to simulate emptying due to gravity. Prior studies did not account for the effect of gravity and the difference in density between ingested bolus

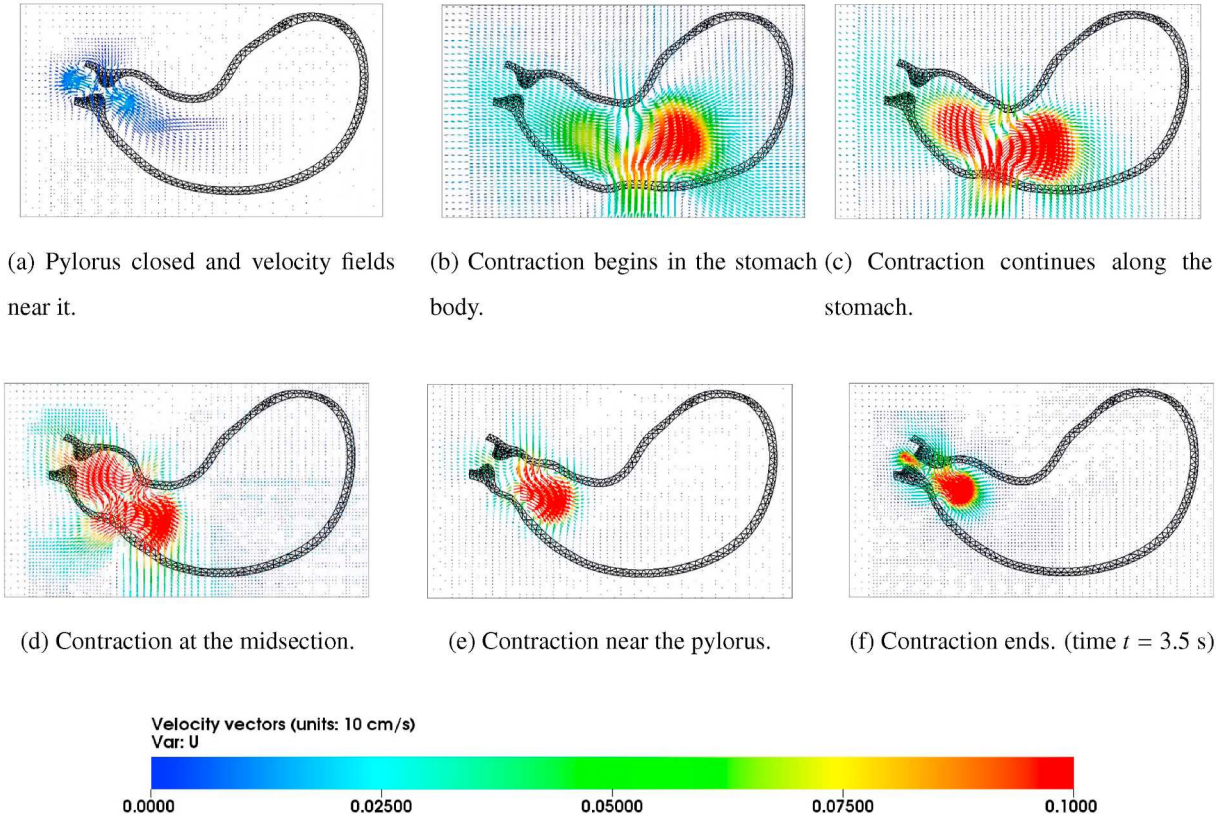

(a) Pylorus closed and velocity fields near it.

(b) Contraction begins in the stomach body.

(c) Contraction continues along the stomach.

(d) Contraction at the midsection.

(e) Contraction near the pylorus.

(f) Contraction ends. (time $t = 3.5$ s)

Fig. 6. Velocity vector fields observed during gastric peristalsis generated by muscular activations summarized in Table 2. Also seen is the generation of a fluid jet due to the contraction wave. Velocity vectors in the first frame show fluid flow around the pylorus as it is being closed.

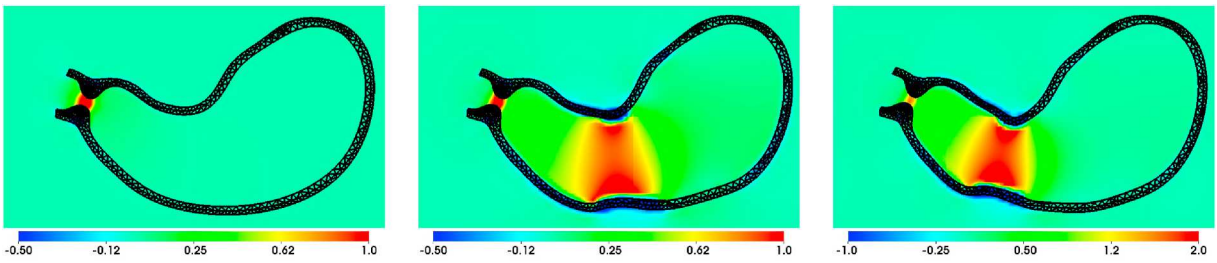

(a) Pressure fields near the closed pylorus. (b) Contraction begins in the stomach body. (c) Contraction continues along the stomach.

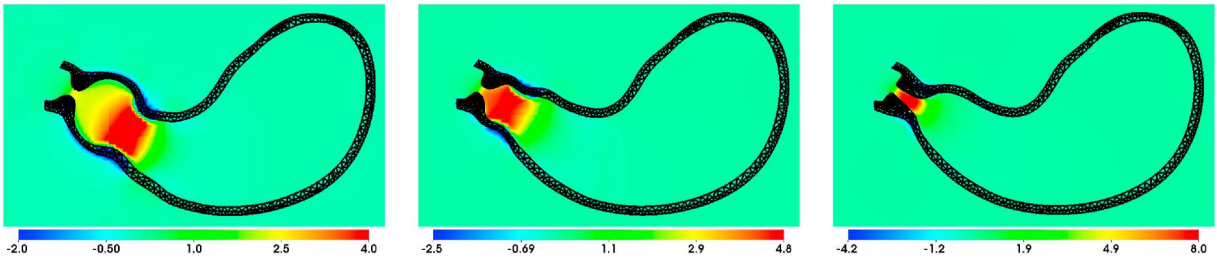

(d) Contraction at the midsection. (e) Contraction near the pylorus. (f) Contraction ends. (time $t = 3.5$ s)

Fig. 7. Pressure fields observed during gastric peristalsis generated by muscular activations summarized in Table 2. The high pressure zones (marked by red contours) force the fluid from these regions to their neighboring regions as seen in the high magnitude velocity vectors in Fig. 6. The pressure fields are represented in their non-dimensional quantities with 1 unit of pressure = 10 Pa.

and the surrounding fluid. In this example, we introduce a pill-shaped bolus (i.e., a cylinder capped at both ends resembling a capsule) with a greater density and viscosity compared to the surrounding fluid. The initial level-set function used to generate the pill-shape is as follows,

$$h = \min\left\{\max\left(\frac{(\mathbf{p}-\mathbf{a})\cdot(\mathbf{b}-\mathbf{a})}{(\mathbf{b}-\mathbf{a})\cdot(\mathbf{b}-\mathbf{a})}, 0.0\right), 1.0\right\}, \tag{14}$$

$$\mathrm{sdf}(\mathbf{p}) = \|(\mathbf{p}-\mathbf{a}) - (\mathbf{b}-\mathbf{a})h\| - r. \tag{15}$$

Here, $\mathbf{p}$ represents the three dimensional coordinates of any point in the domain whose signed distance from the capsule surface needs to be computed. The three-dimensional vectors $\mathbf{a}$ and $\mathbf{b}$ denote the centers of the circles that form the ends of the cylindrical portion of the pill shape. The radius of the cylinder and the spherical volumes that cap the cylinder at both ends are equal and denoted by r. Equation (14) *clamps* the value of h between 0 and 1 depending on the location of $\mathbf{p}$ relative to the ends of the cylinder. This value is then used to compute the signed distance function for all points in the domain using Eq. (15). All points within the capsule region (with a negative level set value) were assigned a density of $1.5\rho_f$ and a dynamic viscosity of $3\mu_f$ where ρ_f and μ_f are material properties of the surrounding ambient fluid taken from previous studies [19]. This formed the initial shape of the bolus with a volume of 3.5 mL, occupying the esophageal lumen before entering the stomach.

The evolution of the bolus as it enters the stomach is shown in Fig. 8. The first instant of Fig. 8 shows the location of the zero-level set as constructed by Eq. (15). For this test case, the active portion of the stomach wall is disabled. This is based on the fact that gastric peristalsis is rarely observed when the volume of fluid entering the stomach is small, as it is specified for this test case. The bolus fully exits the esophagus while the peristaltic contraction just begins traveling over the esophagus. This shows that the difference in density between the bolus and the ambient fluid was sufficient to achieve gravity-induced bolus transport. It must be emphasized that there is a subtle but important difference between the simulation shown here and emptying occurring in a human subject. When food enters the esophagus, the stomach walls expand, allowing its volume to increase in a process called *gastric accommodation*. This leads to a decrease in pressure in the gastric cavity allowing the bolus to enter the stomach. In this test case however, emptying is made possible by leaving the pyloric sphincter open. One can observe the development of greater fluid velocity at this location as the bolus enters the stomach. Due to ambient fluid exiting the stomach cavity through the pylorus, the heavier bolus is able to enter to stomach and break up as shown in Fig. 8. We address this limitation below and future work will be geared towards implementing realistic behavior of the stomach walls to model gastric accommodation.

4.3. Example 3: simulating a transient LES relaxation (tLESR) event and retrograde flow of stomach contents into the esophagus

In this final example showcasing the application of previously developed concepts, we construct a test case for retrograde (reverse) flow of stomach contents into the esophagus. This flow is driven by buoyancy forces due to differences in density. Similar flow patterns occur during commonly observed phenomena like eructation (belching), acid reflux and emesis (vomiting). Under normal conditions, the EGJ remains closed and prevents acidic stomach contents from entering the esophagus and harming its delicate inner mucosal layer. Retrograde flow occurs when this barrier is opened either by infrequent muscular relaxation in a healthy subject or mechanical weakening due to pathological developments like hiatal hernia or a hypotensive LES [44]. There are two primary forces that drive this retrograde flow: 1) greater pressure in the gastric cavity due to contraction or tone in the walls of the fundus, or, 2) differences in density between the confined and ambient fluids, leading to a pressure gradient generated by the buoyancy forces. For this test case, we disable the active component in the stomach walls and consider it to be a simple, hyperelastic container that serves to confine the fluid within its boundaries. Thus, gravitational effects combined with the differences in density lead to retrograde fluid flow.

Modeling this retrograde flow requires three key ingredients: (1) A closed structural barrier that resembles a sphincter at the distal end of

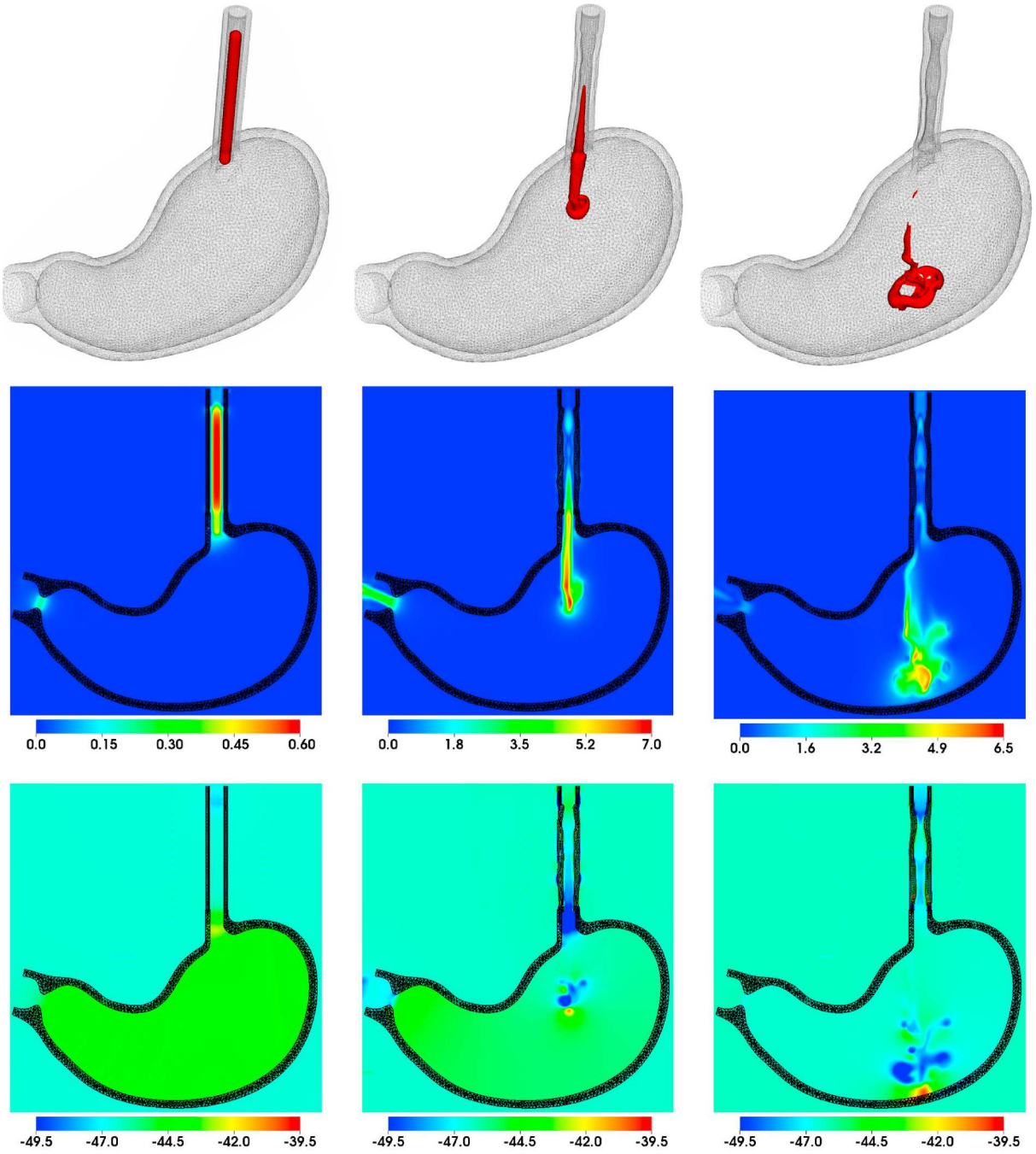

Fig. 8. Gravity-driven bolus emptying into the stomach. Figures in the top row show the evolution of the surface of the bolus as it enters the stomach. This is constructed by visualizing the zero-level set surface in the domain. Figures in the middle and bottom rows show the contours of fluid velocity and pressure, respectively in a two-dimensional plane slicing the esophagus and stomach in half. The velocity and pressure are represented in their non-dimensional form where 1 unit of velocity = 10 cm/s and 1 unit of pressure = 10 Pa.

the esophagus, (2) A lower density fluid resting against this closed barrier, and (3) a controlled opening of the sphincter to allow this fluid to escape into the esophagus. We obtain this configuration by first closing the sphincter as shown in Fig. 9a. The initial configuration of the fluid is that of a spherical bubble in the middle of the gastric cavity. The bubble is then allowed to rise and reach the closed sphincter. The fluid is then allowed to reach steady state as shown in Fig. 9c. After this steady state configuration is reached, the sphincter opening is modeled by increasing the rest length of the circular muscle fibers in the closed segment. A similar behavior occurs during transient lower esophageal sphincter relaxation(tLESR). This spontaneous relaxation of the LES periodically allows air trapped in the stomach to escape [45]. Following this type of opening in the model presented here, the lighter fluid is then able to increase the area of the sphincter and enter the esophageal lumen as shown in Fig. 9f. Thus, this model is able to account for all three features which are necessary to develop future models to study tLESRs, acid reflux and the mechanical competency of the esophagogastric junction to prevent reflux. In addition to visualizing the density field during retrograde flow, we also construct fluid velocity magnitude and pressure contours in Figs. 10 and 11 to provide a complete picture of fluid motion. Pressure contours have been adjusted to exclude the effect of gravity. Without this correction, variation in pressure fields driving

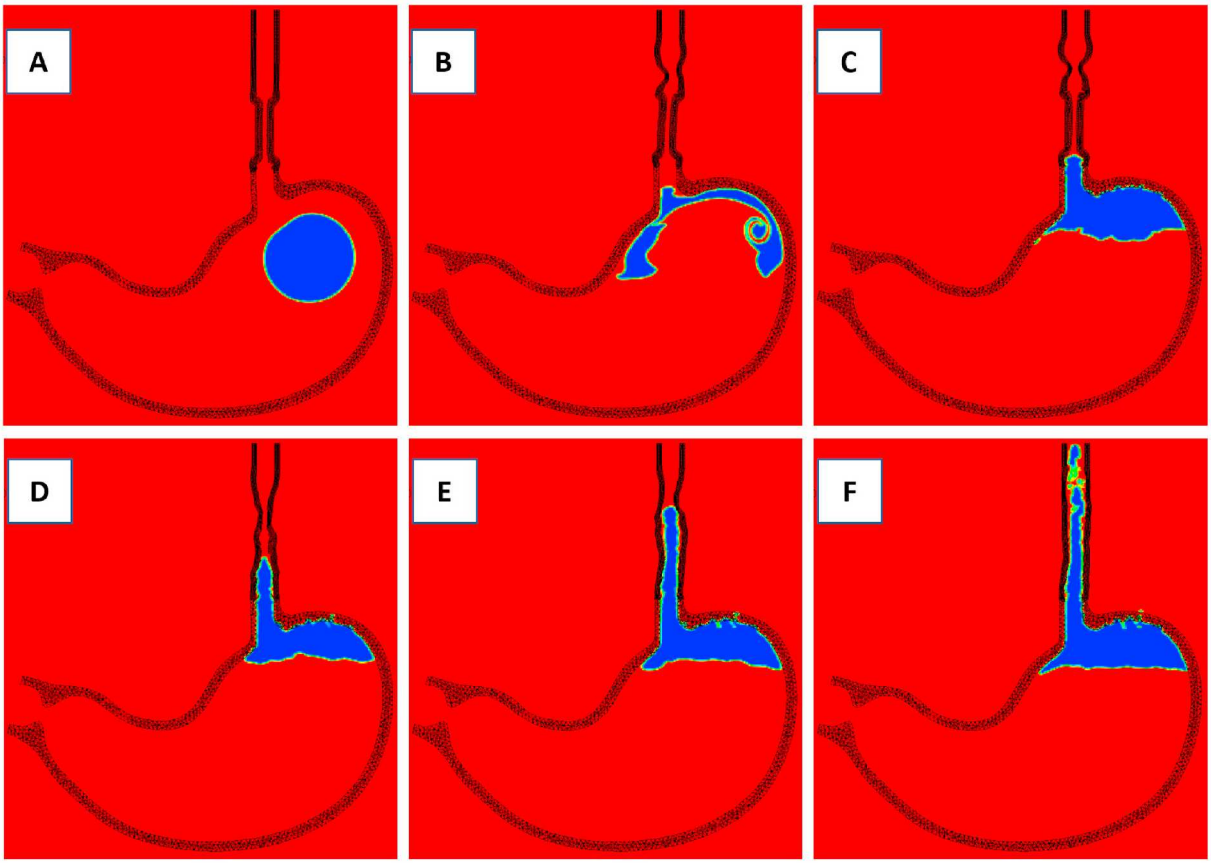

Fig. 9. Retrograde flow of a lower density fluid (ρ = 900 kg/m^3) from the stomach into the esophagus. Ambient fluid is water (ρ = 1000 kg/m^3), shown in red. Figure (c) is a temporary steady state where the fluid has settled in the fundus and prevented from entering the esophagus by the closed sphincter. Figure (d) shows the density field shortly after the sphincter is programmed to open.

flow would not be visible as pressure variations due to increase in the height of the fluid column are far greater.

There are several key things to note about the successful implementation of this model. Observe that the LES does not appear to be fully closed (no physical contact between the walls as seen in Fig. 9a). Due to the delta function kernels used in the immersed boundary method, the fluid-solid interface is smeared. This ensures that although the LES does not *appear* to be closed, it is *effectively* closed because the Lagrangian forcing from the esophagus' walls extends into the lumen and offers some resistance to fluid flow. Another physiological detail that must be emphasized is that the distance between the LES and the stomach was increased to make the physiological problem more amenable for simulation. In reality, the LES spans the region where the stomach meets the cylindrical tube forming the angle of His. Similarly, the effect of surface tension between the two fluids has not been modeled. Finally, the most important limitation of this model was the small difference in density between the ambient and trapped fluid in the stomach. Ideally, the density ratio modeled should be equal to 10^3, reflecting a problem involving air and water. However, this led to significant buoyancy forces being applied on the entire stomach structure causing large, unrealistic deformations. Thus, a smaller density ratio was chosen to develop this test case. This deficiency can be rectified by including the restraining effect of the diaphragm on the stomach and ensuring that the esophagus is filled with air as it is in human subjects. Future modeling attempts will account for these details and treat the contents of the stomach as air and water with the appropriate surface tension effects for a better depiction of the true physical problem.

5. Model limitations and future work

Due to the immense complexity of most organ systems, coupled with limitations on computational resources available, it is challenging for a model to capture all the physics relevant to normal physiologic function. For the gastrointestinal tract in particular, it is not only homogeneous fluid and solid mechanics, but also granular flow, chemical kinetics and tissue electro-mechanical activity that governs overall organ function. The model presented in this work does not account for the absorption and mechanical breakdown of solid food in the stomach due to the pulverizing action of gastric peristalsis. Similarly, most commonly consumed foods are complex non-Newtonian fluids, unlike the fluids modeled in this work. It also does not account for the complex interaction between the structure's strain fields and their influence on intensity of peristalsis and gastric accommodation which normally occurs in the stomach walls as they distend and respond to the amount of food due to distension-induced mechanoreceptors [46,47]. As explained in Sec. 1, models presented by other researchers have accounted for electrical activity or chemical kinetics but no work has been done that accounts for the most important physical interaction in the GI system i.e. between the fluid contents and the elastic structures that modify their flow fields.

Another important but rectifiable limitation of this work is the usage of an idealized stomach and esophagus geometry. The assigned fiber-architecture was also procedurally generated and not based on real clinical imaging. In reality, the esophagus is not a perfectly straight cylinder and the stomach's shape is far more complex than shown in Fig. 2. For the purposes of this study, we chose to construct the 3D model from pictorial representations of the stomach in commonly available literature on human anatomy. Muscle layers were then constructed

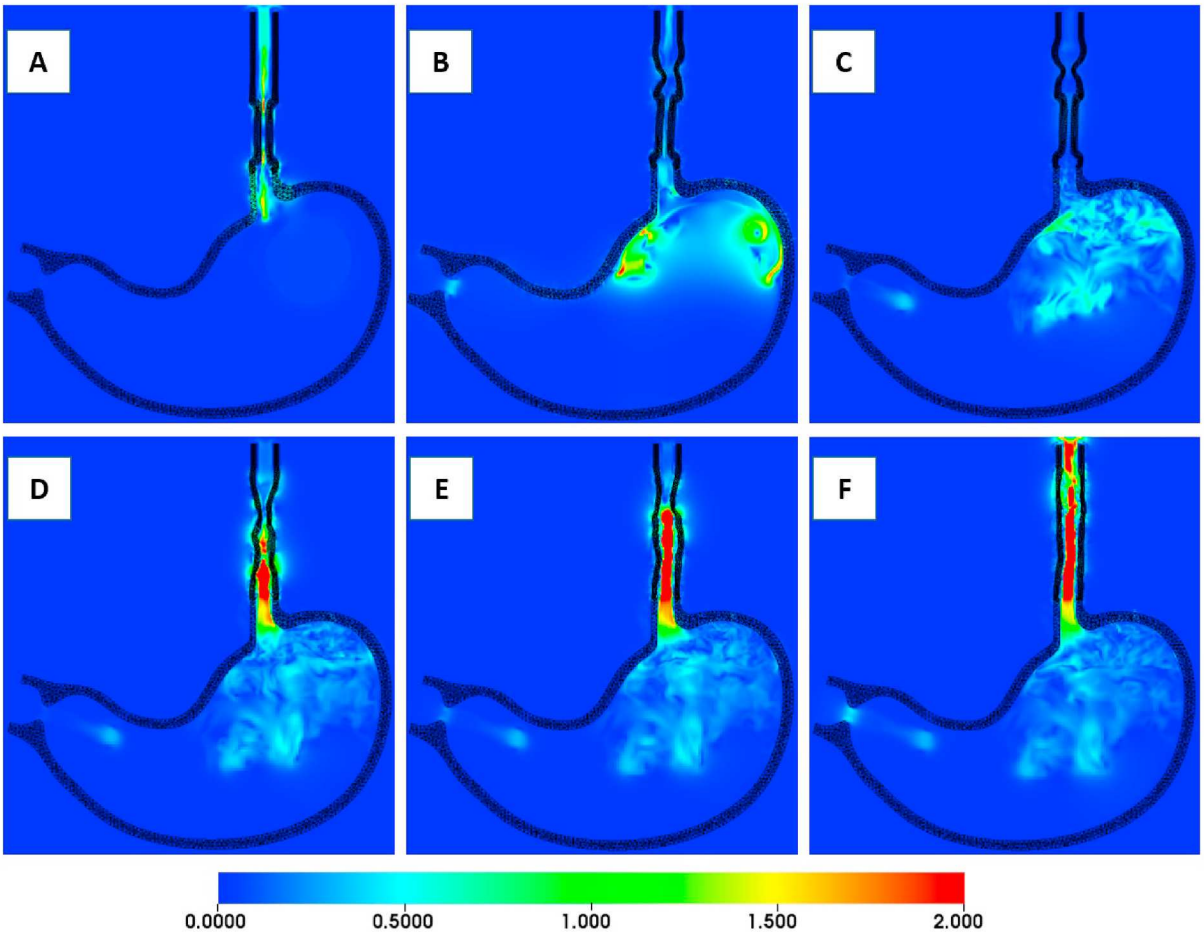

Fig. 10. Velocity magnitude contours observed during retrograde flow of fluid entering the esophageal lumen. Each frame corresponds to the instant shown in Fig. 9. Velocity scale shown below represents 1 unit = 10 cm/s of velocity magnitude. Velocity variation in frame A is due to the closing of the EGJ.

based on rough estimates of muscle thickness and inflating the idealized stomach cavity volume. The oblique muscle layer was not modeled as well. Similar to the esophagus, the stomach has mucosal and submucosal layers with a large amount of gastric folds. These can unfold when the stomach expands to increase its volume. In addition to this, these folds can affect the fluid's velocity profile near the stomach wall. Thus, assuming a smooth inner surface for the stomach wall is another limitation of this study. Ideally, the esophagus and stomach geometry would be obtained from medical imaging of a subject (e.g., MRI or CT scan) and segmenting the data to isolate various muscle layers and generate a realistic 3D structure for simulation. In a future work, we aim to obtain data from 4D-MRI scans [48] and generate patient-specific geometries for improved simulation and analysis. These advanced imaging technologies also enable detailed visualization of flow within the gastric lumen. Measurements collected from these studies will be essential to validate the model against experimental data obtained from control subjects. For muscle fiber architecture, diffusion tensor imaging [49,50] or sectioning microscopy [51,52] has been used to find the orientation of individual fibers. However, for future studies, we aim to stick to rule-based algorithms [53] to assign fiber architecture and move to medical imaging-based approaches when some of the more pressing limitations have been addressed. Alongside these factors, downstream pressure conditions and non-uniform fiber architecture can influence the speed of the bolus as it travels along the lumen. Accounting for these details is essential to ensure that estimated time for complete bolus transport accurately reflects observed physiology. By accounting for all these factors, continuous improvement of the above model will enable validation of numerical results with measurements obtained from clinical subjects.

In addition to the technical limitations mentioned above, it must be noted that there were a few features of the esophagogastric junction (EGJ) that were not fully captured in the present model. The EGJ is the location where the esophagus continues on into the stomach. It is an anatomically complex region with two important components: 1) an intrinsic sphincter, commonly known as the lower esophageal sphincter (LES), and, 2) an extrinsic sphincter which consists of the crural diaphragm and other surrounding structures at the EGJ [54]. The combination of these two structures forms the primary barrier that prevents stomach acids from entering the esophagus. In the model presented above, the LES is adequately captured by the circular muscle fiber architecture which can be programmed to contract or relax to allow fluid to enter the stomach. However, the extrinsic sphincter which consists of sling fibers from the crural diaphragm has not been modeled. These fibers wrap around the esophagus and are responsible for creating a significant asymmetry in the pressure profile at the EGJ [55]. In addition to these fibers, an additional structure called the phrenoesophageal ligament (PEL) is responsible for tethering the esophagus to the diaphragm. This tethering adds a significant amount of longitudinal tension to the esophagus which can affect the motion of the EGJ during emptying or reflux. This tension is primarily responsible for the esophagus returning to its original configuration after longitudinal muscle contraction [56]. The presence of these two elements, i.e. the PEL and sling fibers, is particularly important in the context of gastroesophageal reflux disease (GERD) and hiatal hernia as their integrity is compromised in this disease state. As such, future efforts will be acutely directed towards developing a detailed model of the PEL and gastric sling fibers to

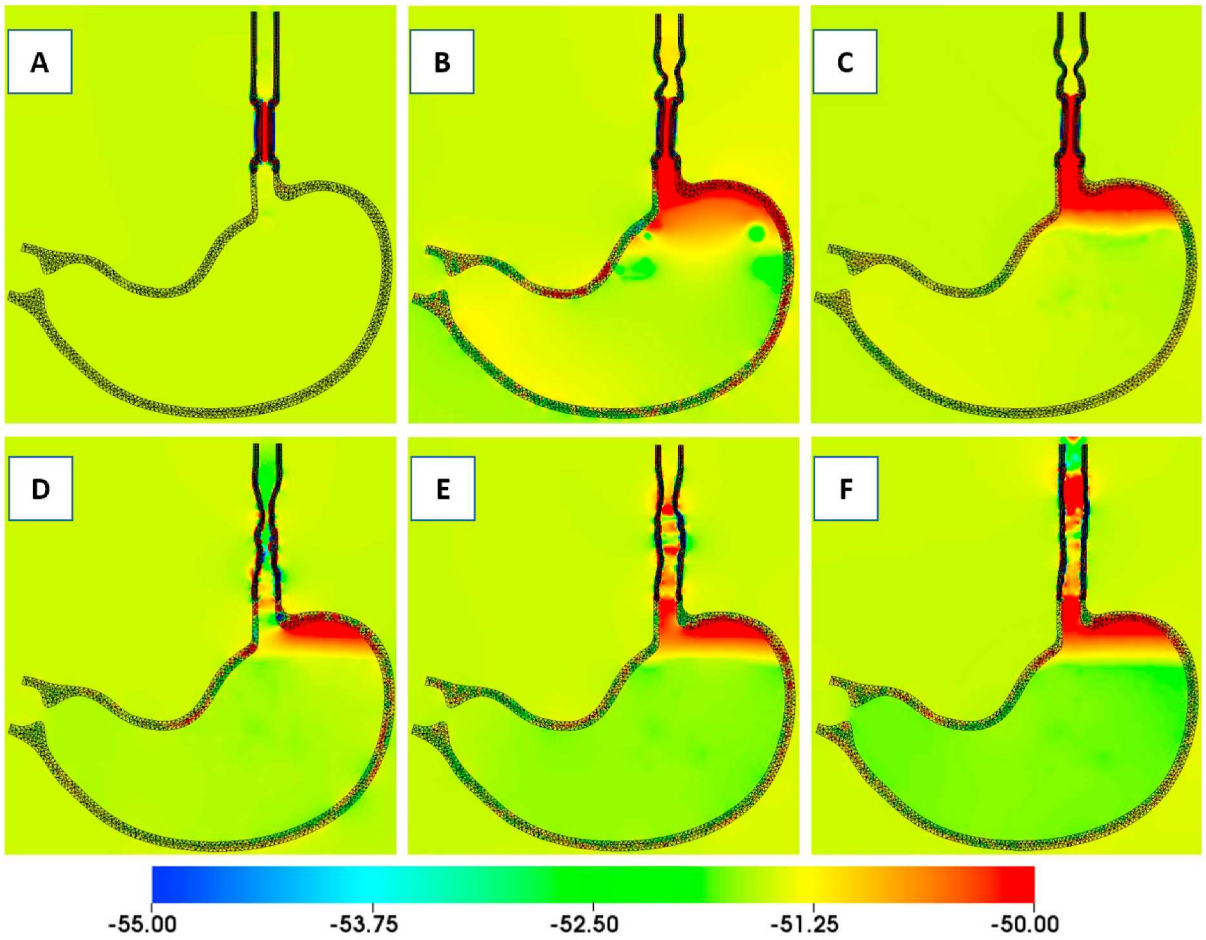

Fig. 11. Variation of pressure in the domain during retrograde flow. Hydrostatic component of pressure has been removed to better visualize pressure fields that drive fluid flow. As such, the lower density fluid that is confined in the stomach cavity appears to be at a higher pressure value. Once the EGJ opens, fluid enters the esophageal lumen. Pressure contours represent 10 Pa of pressure for 1 unit value.

properly capture their overall effect on EGJ function in normal and pathological scenarios.

Funding data

- National Institutes of Health (NIDDK grants DK079902 & DK117824 to JEP; Funder ID: 10.13039/100000062).
- National Science Foundation (OAC grants 1450374 & 1931372 to NAP; Funder ID: 10.13039/100000105).

Declaration of competing interest

D. A. Carlson, P. J. Kahrilas, and J. E. Pandolfino hold shared intellectual property rights and ownership surrounding FLIP panometry systems, methods, and apparatus with Medtronic Inc.

D. A. Carlson: Medtronic (Speaking, Consulting).

W. Kou: Crospon, Inc. (Consulting).

P. J. Kahrilas: Ironwood (Consulting), R. Benckiser (Consulting).

J. E. Pandolfino: Crospon, Inc. (stock options), Given Imaging (Consultant, Grant, Speaking), Sandhill Scientific (Consulting, Speaking), Takeda (Speaking), Astra Zeneca (Speaking), Medtronic (Speaking, Consulting), Torax (Speaking, Consulting), Ironwood (Consulting), Impleo (Grant).

S. Acharya, S. Halder, and N. A. Patankar: No conflicts of interest.

Acknowledgments

This research was supported in part through the computational resources and staff contributions provided for the Quest high performance computing facility at Northwestern University which is jointly supported by the Office of the Provost, the Office for Research, and Northwestern University Information Technology. This work also used the Extreme Science and Engineering Discovery Environment (XSEDE) clusters Comet, at the San Diego Supercomputer Center (SDSC) and Bridges-2, at the Pittsburgh Supercomputing Center (PSC) through allocation TG-ASC170023, which is supported by National Science Foundation grant number ACI-1548562 [57].

Appendix A. Supplementary data

Supplementary data to this article can be found online at https://doi.org/10.1016/j.compbiomed.2021.104948.

References

[1] M. Ferrua, R. Singh, Modeling the fluid dynamics in a human stomach to gain insight of food digestion, J. Food Sci. 75 (7) (2010) R151–R162, https://doi.org/10.1111/j.1750-3841.2010.01748.x.

[2] M.J. Ferrua, R.P. Singh, Understanding the fluid dynamics of gastric digestion using computational modeling, Proc. Food Sci. 1 (2011) 1465–1472, https://doi.org/10.1016/j.profoo.2011.09.217.

[3] A. Pal, K. Indireshkumar, W. Schwizer, B. Abrahamsson, M. Fried, J.G. Brasseur, Gastric flow and mixing studied using computer simulation, Proc. Roy. Soc. Lond. B Biol. Sci. 271 (1557) (2004) 2587–2594, https://doi.org/10.1098/rspb.2004.2886.

[4] M. Peirlinck, N. Debusschere, F. Iannaccone, P.D. Siersema, B. Verhegghe, P. Segers, M.D. Beule, An in silico biomechanical analysis of the stent–esophagus interaction, Biomech. Model. Mechanobiol. 17 (1) (2017) 111–131, https://doi.org/10.1007/s10237-017-0948-9.

[5] R. Yassi, L. Cheng, V. Rajagopal, M. Nash, J. Windsor, A. Pullan, Modeling of the mechanical function of the human gastroesophageal junction using an anatomically realistic three-dimensional model, J. Biomech. 42 (11) (2009) 1604–1609, https://doi.org/10.1016/j.jbiomech.2009.04.041.

[6] Y. Imai, I. Kobayashi, S. Ishida, T. Ishikawa, M. Buist, T. Yamaguchi, Antral recirculation in the stomach during gastric mixing, Am. J. Physiol. Gastrointest. Liver Physiol. 304 (5) (2013) G536–G542, https://doi.org/10.1152/ajpgi.00350.2012.

[7] A. Pal, J.G. Brasseur, B. Abrahamsson, A stomach road or "magenstrasse" for gastric emptying, J. Biomech. 40 (6) (2007) 1202–1210, https://doi.org/10.1016/j.jbiomech.2006.06.006.

[8] H. Gregersen, Biomechanics of the Gastrointestinal Tract, Springer London, 2003, https://doi.org/10.1007/978-1-4471-3742-9.

[9] F. Karkossa, S. Klein, Individualized in vitro and in silico methods for predicting in vivo performance of enteric-coated tablets containing a narrow therapeutic index drug, Eur. J. Pharm. Biopharm. 135 (2019) 13–24, https://doi.org/10.1016/j.ejpb.2018.12.004.

[10] P.-C. Chiang, K. Nagapudi, M.J. Dolton, J. Liu, Exploring multicompartment plug flow–based model approach in biopharmaceutics: impact of stomach setting and the estimation of the fraction absorbed of orally administered basic drugs, J. Pharmaceut. Sci. 109 (3) (2020) 1261–1269, https://doi.org/10.1016/j.xphs.2019.11.021.

[11] P. Paixão, M. Bermejo, B. Hens, Y. Tsume, J. Dickens, K. Shedden, N. Salehi, M. J. Koenigsknecht, J.R. Baker, W.L. Hasler, R. Lionberger, J. Fan, J. Wysocki, B. Wen, A. Lee, A. Frances, G.E. Amidon, A. Yu, G. Benninghoff, R. Löbenberg, A. Talattof, D. Sun, G.L. Amidon, Gastric emptying and intestinal appearance of nonabsorbable drugs phenol red and paromomycin in human subjects: a multi-compartment stomach approach, Eur. J. Pharm. Biopharm. 129 (2018) 162–174, https://doi.org/10.1016/j.ejpb.2018.05.033.

[12] B. Hens, M.B. Bolger, Application of a dynamic fluid and pH model to simulate intraluminal and systemic concentrations of a weak base in GastroPlus™, J. Pharmaceut. Sci. 108 (1) (2019) 305–315, https://doi.org/10.1016/j.xphs.2018.10.041.

[13] S. Brandstaeter, S. L. Fuchs, R. C. Aydin, C. J. Cyron, Mechanics of the stomach: a review of an emerging field of biomechanics, GAMM-Mitteilungen 42 (3). doi:10.1002/gamm.201900001.

[14] L.K. Cheng, P. Du, G. O'Grady, Mapping and modeling gastrointestinal bioelectricity: from engineering bench to bedside, Physiology 28 (5) (2013) 310–317, https://doi.org/10.1152/physiol.00022.2013.

[15] A. Pullan, L. Cheng, R. Yassi, M. Buist, Modelling gastrointestinal bioelectric activity, Prog. Biophys. Mol. Biol. 85 (2–3) (2004) 523–550, https://doi.org/10.1016/j.pbiomolbio.2004.02.003.

[16] H. Miki, T. Okuyama, S. Kodaira, Y. Luo, T. Takagi, T. Yambe, T. Sato, Artificial-esophagus with peristaltic motion using shape memory alloy, Int. J. Appl. Electromagn. Mech. 33 (1–2) (2010) 705–711, https://doi.org/10.3233/JAE-2010-1176.

[17] P. Kahrilas, W. Dodds, W. Hogan, Effect of peristaltic dysfunction on esophageal volume clearance, Gastroenterology 94 (1) (1988) 73–80, https://doi.org/10.1016/0016-5085(88)90612-9.

[18] C.E. Pope, The esophagus for the nonesophagologist, Am. J. Med. 103 (5) (1997) 19S–22S, https://doi.org/10.1016/s0002-9343(97)00315-x.

[19] W. Kou, B.E. Griffith, J.E. Pandolfino, P.J. Kahrilas, N.A. Patankar, A continuum mechanics-based musculo-mechanical model for esophageal transport, J. Comput. Phys. 348 (2017) 433–459, https://doi.org/10.1016/j.jcp.2017.07.025.

[20] W. Kou, J.E. Pandolfino, P.J. Kahrilas, N.A. Patankar, Could the peristaltic transition zone be caused by non-uniform esophageal muscle fiber architecture? a simulation study, Neuro Gastroenterol. Motil. 29 (6) (2017), e13022, https://doi.org/10.1111/nmo.13022.

[21] W. Kou, J.E. Pandolfino, P.J. Kahrilas, N.A. Patankar, Studies of abnormalities of the lower esophageal sphincter during esophageal emptying based on a fully coupled bolus–esophageal–gastric model, Biomech. Model. Mechanobiol. 17 (4) (2018) 1069–1082, https://doi.org/10.1007/s10237-018-1014-y.

[22] D. Boffi, L. Gastaldi, L. Heltai, C.S. Peskin, On the hyper-elastic formulation of the immersed boundary method, Comput. Methods Appl. Mech. Eng. 197 (25–28) (2008) 2210–2231, https://doi.org/10.1016/j.cma.2007.09.015, https://doi.org/10.1016/j.cma.2007.09.015.

[23] B.E. Griffith, X. Luo, Hybrid finite difference/finite element immersed boundary method, Int. J. Numer. Methods Biomed. Eng. 33 (12) (2017), e2888, https://doi.org/10.1002/cnm.2888.

[24] B. Vadala-Roth, S. Acharya, N.A. Patankar, S. Rossi, B.E. Griffith, Stabilization approaches for the hyperelastic immersed boundary method for problems of large-deformation incompressible elasticity, Comput. Methods Appl. Mech. Eng. 365 (2020) 112978, https://doi.org/10.1016/j.cma.2020.112978.

[25] N. Nangia, N.A. Patankar, A.P.S. Bhalla, A DLM immersed boundary method based wave-structure interaction solver for high density ratio multiphase flows, J. Comput. Phys. 398 (2019) 108804, https://doi.org/10.1016/j.jcp.2019.07.004.

[26] B.E. Griffith, An accurate and efficient method for the incompressible Navier–Stokes equations using the projection method as a preconditioner, J. Comput. Phys. 228 (20) (2009) 7565–7595, https://doi.org/10.1016/j.jcp.2009.07.001, https://doi.org/10.1016/j.jcp.2009.07.001.

[27] N. Nangia, B.E. Griffith, N.A. Patankar, A.P.S. Bhalla, A robust incompressible Navier-Stokes solver for high density ratio multiphase flows, J. Comput. Phys. 390 (2019) 548–594, https://doi.org/10.1016/j.jcp.2019.03.042.

[28] B. E. Griffith, IBAMR: an Adaptive and Distributed-memory Parallel Implementation of the Immersed Boundary Method. URL https://ibamr.github.io/about.

[29] R. Anderson, W. Arrighi, N. Elliott, B. Gunney, R. Hornung, Samrai Concepts and Software Design, Lawrence Livermore Nat. Lab. Rept. LLNL-SM-617092-DRAFT..

[30] B.S. Kirk, J.W. Peterson, R.H. Stogner, G.F. Carey, libmesh: a c++ library for parallel adaptive mesh refinement/coarsening simulations, Eng. Comput. 22 (3–4) (2006) 237–254.

[31] S. Balay, S. Abhyankar, M. Adams, J. Brown, P. Brune, K. Buschelman, L. Dalcin, A. Dener, V. Eijkhout, W. Gropp, et al., Petsc Users Manual..

[32] R.L. Drake, in: Gray's Anatomy for Students, fourth ed., Elsevier, Philadelphia, MO, 2019.

[33] R.P. Smith, F.H. Netter, C.A.G. Machado, F.H. Netter (Eds.), The Netter Collection of Medical Illustrations, second ed., Elsevier, Philadelphia, PA, 2011.

[34] A. Gnerucci, P. Faraoni, S. Calusi, F. Fusi, G. Romano, Influence of stomach mucosa tissue on the efficacy of intragastric antibacterial PDT, Photochem. Photobiol. Sci. 19 (1) (2020) 34–39, https://doi.org/10.1039/c9pp00315k.

[35] C. Geuzaine, J.-F. Remacle, Gmsh, A 3-d finite element mesh generator with built-in pre- and post-processing facilities, Int. J. Numer. Methods Eng. 79 (11) (2009) 1309–1331, https://doi.org/10.1002/nme.2579.

[36] M.J. Ferrua, Z. Xue, R. Paul Singh, On the kinematics and efficiency of advective mixing during gastric digestion – a numerical analysis, J. Biomech. 47 (15) (2014) 3664–3673, https://doi.org/10.1016/j.jbiomech.2014.09.033.

[37] k. schulze, Imaging and modelling of digestion in the stomach and the duodenum, Neuro Gastroenterol. Motil. 18 (3) (2006) 172–183, https://doi.org/10.1111/j.1365-2982.2006.00759.x.

[38] K. Deeg, G. Zeilinger, B. Böwing, U. Brandl, Sonographische diagnose der hypertrophen pylorusstenose im kindesalter, Ultraschall der Med. 6 (6) (2008) 320–324, https://doi.org/10.1055/s-2007-1006079.

[39] D. Liebermann-Meffert, M. Allgöwer, P. Schmid, A.L. Blum, Muscular equivalent of the lower esophageal sphincter, Gastroenterology 76 (1) (1979) 31–38, https://doi.org/10.1016/s0016-5085(79)80124-9, https://doi.org/10.1016/s0016-5085(79)80124-9.

[40] M. Bouchard, M.F. McAleer, G. Starkschall, Impact of gastric filling on radiation dose delivered to gastroesophageal junction tumors, Int. J. Radiat. Oncol. Biol. Phys. 77 (1) (2010) 292–300, https://doi.org/10.1016/j.ijrobp.2009.08.026.

[41] W. Yang, T.C. Fung, K.S. Chian, C.K. Chong, 3d mechanical properties of the layered esophagus: experiment and constitutive model, J. Biomech. Eng. 128 (6) (2006) 899–908, https://doi.org/10.1115/1.2354206.

[42] Y. Bao, A. Donev, B.E. Griffith, D.M. McQueen, C.S. Peskin, An immersed boundary method with divergence-free velocity interpolation and force spreading, J. Comput. Phys. 347 (2017) 183–206, https://doi.org/10.1016/j.jcp.2017.06.041, https://doi.org/10.1016/j.jcp.2017.06.041.

[43] R.K. Avvari, Theoretical modeling of the resistance to gastric emptying and duodenogastric reflux due to pyloric motility alone, presuming antral and duodenal quiescence, J. Theor. Biol. 508 (2021) 110460, https://doi.org/10.1016/j.jtbi.2020.110460, https://doi.org/10.1016/j.jtbi.2020.110460.

[44] P. Gor, Y. Li, S. Munigala, A. Patel, A. Bolkhir, C.P. Gyawali, Interrogation of esophagogastric junction barrier function using the esophagogastric junction contractile integral: an observational cohort study, Dis. Esophagus 29 (7) (2015) 820–828, https://doi.org/10.1111/dote.12389, https://doi.org/10.1111/dote.12389.

[45] H.I. Kim, S.J. Hong, J.P. Han, J.Y. Seo, K.H. Hwang, H.J. Maeng, T.H. Lee, J.S. Lee, Specific movement of esophagus during transient lower esophageal sphincter relaxation in gastroesophageal reflux disease, J. Neurogastroenterol. Motil. 19 (3) (2013) 332–337, https://doi.org/10.5056/jnm.2013.19.3.332, https://doi.org/10.5056/jnm.2013.19.3.332.

[46] T. Takeda, T. Nabae, G. Kassab, J. Liu, R.K. Mittal, Oesophageal wall stretch: the stimulus for distension induced oesophageal sensation, Neuro Gastroenterol. Motil. 16 (6) (2004) 721–728, https://doi.org/10.1111/j.1365-2982.2004.00620.x.

[47] J.D. Barlow, H. Gregersen, D.G. Thompson, Identification of the biomechanical factors associated with the perception of distension in the human esophagus, Am. J. Physiol. Gastrointest. Liver Physiol. 282 (4) (2002) G683–G689, https://doi.org/10.1152/ajpgi.00134.2001.

[48] Z. Stankovic, B. D. Allen, J. Garcia, K. B. Jarvis, M. Markl, 4d flow imaging with mri, Cardiovasc. Diagn. Ther. 4 (2). doi:10.3978/j.issn.2223-3652.2014.01.02..

[49] D. Liao, H. Gregersen, P. Agger, C. Laustsen, S. Ringgaard, H. Stødkilde-Jørgensen, J. Zhao, 3d reconstruction and fiber quantification in the pig lower esophageal sphincter region using in vitro diffusion tensor imaging, Biomed. Phys. Eng. Express 4 (2) (2018), 025002, https://doi.org/10.1088/2057-1976/aa976e.

[50] R.J. Gilbert, T.A. Gaige, R. Wang, T. Benner, G. Dai, J.N. Glickman, V.J. Wedeen, Resolving the three-dimensional myoarchitecture of bovine esophageal wall with diffusion spectrum imaging and tractography, Cell Tissue Res. 332 (3) (2008) 461–468, https://doi.org/10.1007/s00441-008-0601-0.

[51] A. Zifan, D. Kumar, L. K. Cheng, R. K. Mittal, Three-dimensional myoarchitecture of the lower esophageal sphincter and esophageal hiatus using optical sectioning microscopy, Sci. Rep. 7 (1). doi:10.1038/s41598-017-13342-y..

[52] R. Yassi, L. Cheng, S. Al-Ali, G. Sands, D. Gerneke, I. LeGrice, A. Pullan, J. Windsor, Three-dimensional high-resolution reconstruction of the human gastro-oesophageal junction, Clin. Anat. (2010), https://doi.org/10.1002/ca.20941. NA–NA.

[53] J.D. Bayer, R.C. Blake, G. Plank, N.A. Trayanova, A novel rule-based algorithm for assigning myocardial fiber orientation to computational heart models, Ann.

Biomed. Eng. 40 (10) (2012) 2243–2254, https://doi.org/10.1007/s10439-012-0593-5.

[54] J. Tack, J.E. Pandolfino, Pathophysiology of gastroesophageal reflux disease, Gastroenterology 154 (2) (2018) 277–288, https://doi.org/10.1053/j.gastro.2017.09.047.

[55] R.K. Mittal, A. Zifan, D. Kumar, M. Ledgerwood-Lee, E. Ruppert, G. Ghahremani, Functional morphology of the lower esophageal sphincter and crural diaphragm determined by three-dimensional high-resolution esophago-gastric junction pressure profile and CT imaging, Am. J. Physiol. Gastrointest. Liver Physiol. 313 (3) (2017) G212–G219, https://doi.org/10.1152/ajpgi.00130.2017.

[56] C.T. Bombeck, D.H. Dillard, L.M. Nyhus, Muscular anatomy of the gastroesophageal junction and role of phrenoesophageal ligament: autopsy study of sphincter mechanism, Ann. Surg. 164 (4) (1966) 643–654, https://doi.org/10.1097/00000658-196610000-00011.

[57] J. Towns, T. Cockerill, M. Dahan, I. Foster, K. Gaither, A. Grimshaw, V. Hazlewood, S. Lathrop, D. Lifka, G.D. Peterson, R. Roskies, J.R. Scott, N. Wilkins-Diehr, XSEDE: accelerating scientific discovery, Comput. Sci. Eng. 16 (5) (2014) 62–74, https://doi.org/10.1109/MCSE.2014.80.